SUPPLEMENTARY INFORMATION FOR

Shells in CO₂ clusters

John W. Niman,[a] Benjamin S. Kamerin,[a] Vitaly V. Kresin,[a] Jan Krohn,[b]

Ruth Signorell,[b] Roope Halonen,[c] and Klavs Hansen[c,d]

[a] *Department of Physics and Astronomy, University of Southern California,*
Los Angeles, CA 90089-0484, USA

[b] *Laboratory of Physical Chemistry, ETH Zürich, Vladimir-Prelog Weg 2, CH-8093 Zürich, Switzerland*

[c] *Center for Joint Quantum Studies and Department of Physics, School of Science, Tianjin University,*
92 Weijin Road, Tianjin 300072, China

[d] *School of Physical Science and Technology, Lanzhou University, Lanzhou 730000, China*

Contents

S-I. Mass spectrum baseline subtraction and peak integration

Three sample time-of-flight spectra, with their time axes converted to corresponding mass, are shown in Fig. S1. The first step in processing them involves identifying and subtracting a constant baseline. As illustrated in Fig. S2, the collected spectra extend far beyond the range shown above. It is safe to assume that the distant points contain no actual cluster signal and therefore represent the baseline. We extract the last thousand points from the record and use their average as the baseline. This value is then subtracted channel-by-channel from the data. A spectrum after baseline subtraction is shown in Fig. S3.

Subsequently, two additional corrections are applied. The first is a Jacobian factor used in a transformation from the time-of-flight variable to the mass variable. This involves a division of the spectrum by $N^{1/2}$. The second one accounts for the cluster size dependence of the photoioniza-
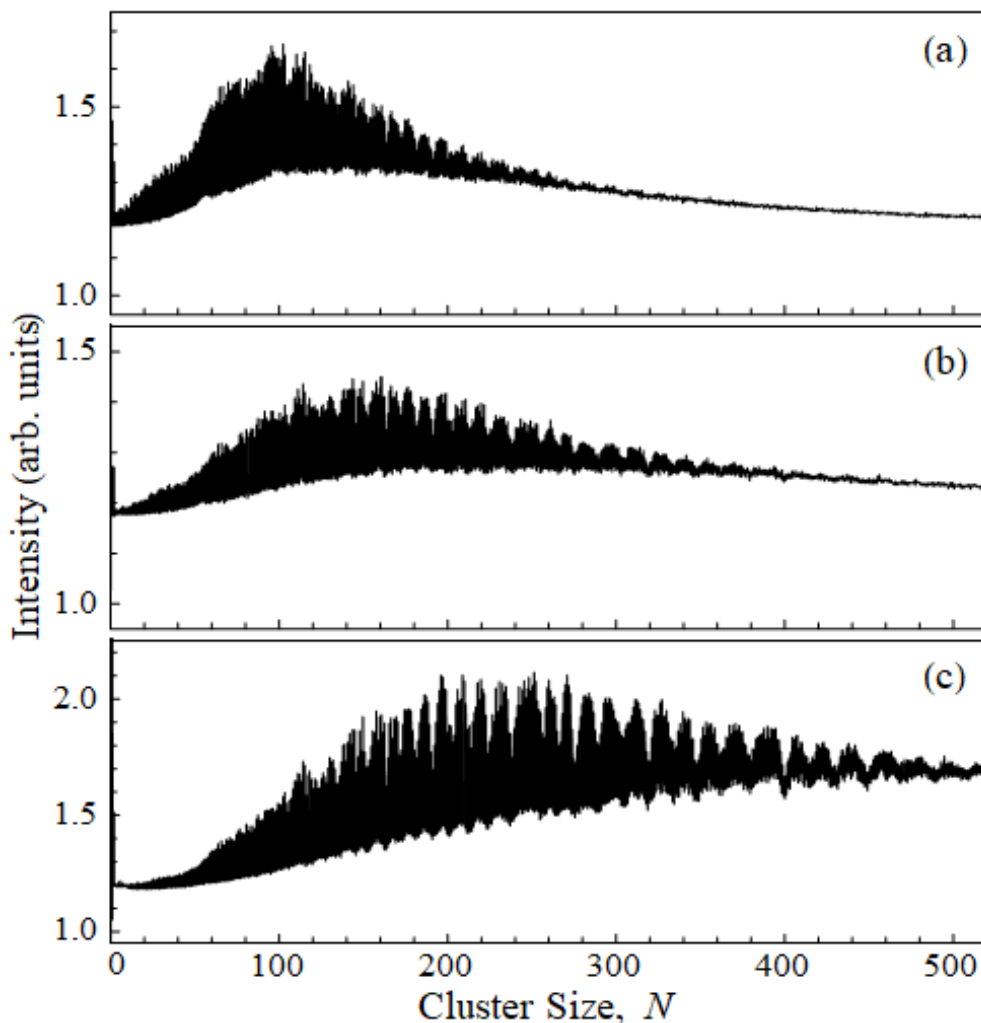
Fig. S1. Raw time-of-flight spectra of CO_2 clusters for three different experimental conditions. (Spectra are reproduced from data presented in Ref. S1.) The mass spectra in Fig. 2 of the main text are derived from these plots following the procedure described in this section.

tion cross section via an additional division by N. The net effect is a pointwise division of the spectra (such as that in Fig. S3) by $N^{3/2}$. The final outcome is illustrated in Fig. 2 in the main text.

Further potential corrections, such as the detector conversion efficiency or other size dependent detection biases, were not included. It is crucial to emphasize that any smooth abundance variations are always removed in the next step, described in Section S-II, and therefore impact neither the stability functions derived there nor any subsequent portion of the analysis. This point follows rigorously from the analysis procedure, and has been verified for the present data.

Following the above corrections, peaks are detected using *Mathematica*'s `FindPeaks` function, with care taken to ensure that exactly one peak is identified for each $(CO_2)_N$ cluster. Fig. S4 shows an example of peaks identified in a baseline-subtracted and corrected spectrum.

Once the $(CO_2)_N$ peak positions are identified, their intensities are determined by numerical integration of a linear interpolation of the data points between the region defined by the midpoints between consecutive peaks. Since there is some variability in where the maxima are determined in the mass spectrum, it is important to normalize the integrated intensity by the distance between the consecutive midpoints. Each integrated intensity is then assigned to an integer value of N corresponding to the cluster size. Variations of this method of peak integration were tried and found to yield similar results. A sample integrated mass spectrum is shown in Fig. S5.
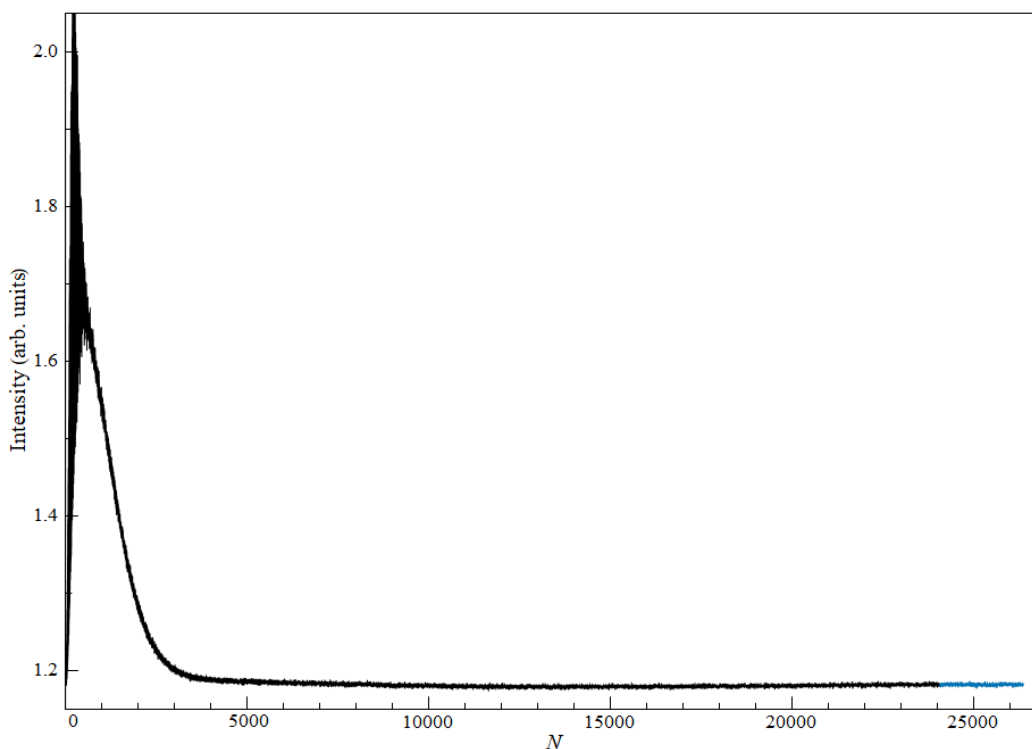
Fig. S2. Full time-of-flight mass spectrum of CO_2 clusters with points used to construct the baseline function visible in blue at the far end. This plot is an extension of Fig. S1(c). (Spectra are reproduced from data presented in Ref. S1.)
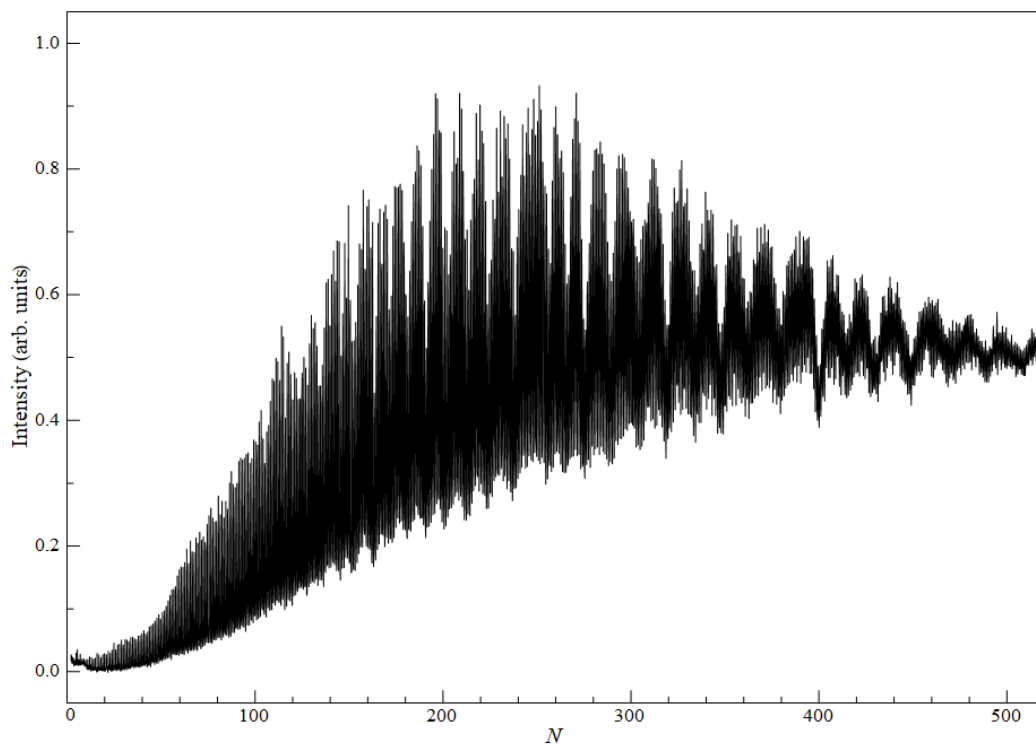
Fig. S3. The spectrum from Fig. S1(c) after subtraction of the baseline determined from the region highlighted in Fig. S2. (Spectra are reproduced from data presented in Ref. S1.)
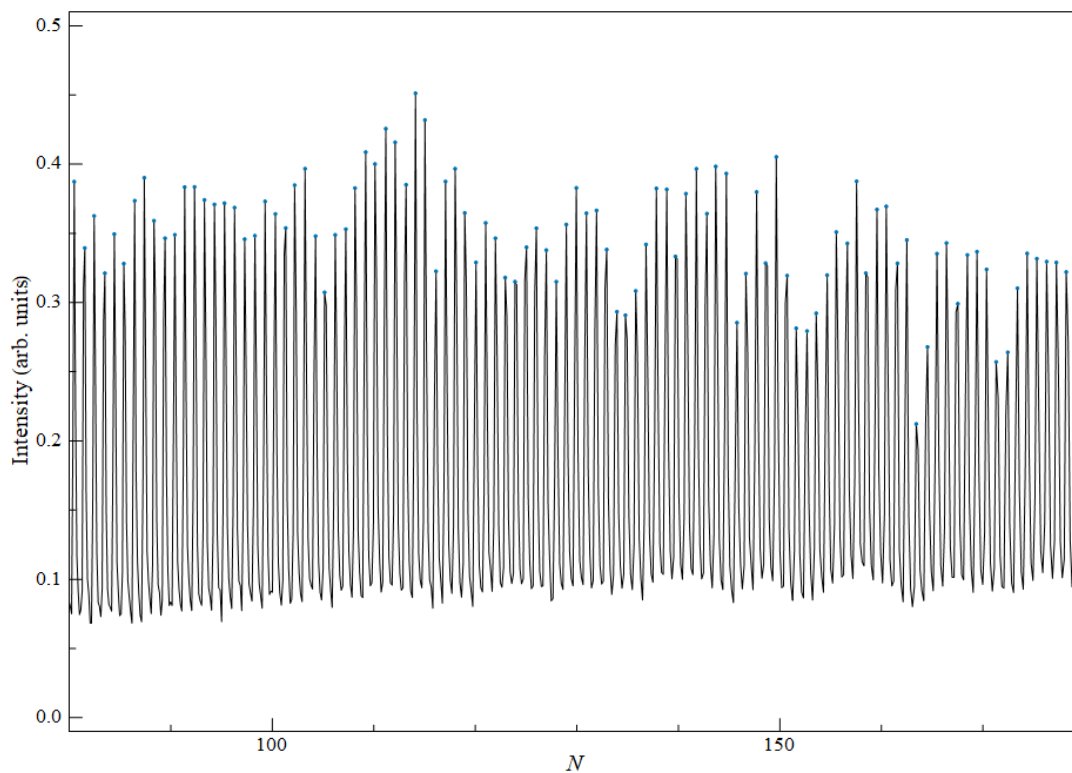
Fig. S4. Peaks identified in a segment of the mass spectrum from Fig. 2(c) in the main text.

S-II. Cluster stability functions

The peak-integrated mass spectra, I_N, are used to generate the "cluster stability functions," $(I_N/\tilde{I}_N)$, which exhibit the size-to-size intensity variations deriving from intrinsic cluster properties. The function $\tilde{I}_N$ represents a smooth envelope of the abundance distribution. Since it depends on the source conditions, it is determined separately for each spectrum by means of smoothing the abundance function itself, as described below.

The procedure used here has strong analogies to the determination of shell structure in the field of nuclear physics by means of the so-called Strutinski shell correction method. It is not limited to nuclei and has been applied to studies of cluster shell and supershell structure as well.[S2,S3]

The smoothing is accomplished by convolution of the abundance spectrum with Gaussian functions, as given by Eq. (1) in the main text. The denominator of this equation normalizes the weight to unity. As mentioned in the main text, the Gaussians' width is set to $w_N = 4N^{1/3}$. This $N^{1/3}$ variation is selected because it matches that of the structures appearing in the mass spectra. Setting the coefficient to 4 was found to provide sufficiently broad averaging without washing out the size variation of $\tilde{I}_N$. Other smoothing choices are possible, for example the use of spline functions.[S3]

To avoid asymmetric averaging at the high mass end of the spectra, we fit the falling edge of the spectra to an exponentially decreasing function of the form $\alpha e^{-\beta N}$, extend the spectrum and use this for the determination of $\tilde{I}_N$. These extensions are smooth and therefore will not give rise to any spurious signals. We also attempted to fit the tail of the spectra to a pseudo-Voigt function with a sigmoidally varying width parameter,[S4] and found similar results to using the decaying exponential function. The following analysis and the results in the main text utilize the fit to the exponentially decreasing function for simplicity.

A single convolution of this type is not sufficient to remove all traces of the envelope function, and the procedure is therefore repeated twice more, using the preceding $\tilde{I}_N$ as the input spectrum. The iterative process leads to stability functions which oscillate about unity.

Fig. S5 shows such a final envelope function $\tilde{I}_N$ superimposed onto the integrated mass spectrum. This plot is also shown in Fig. 4(c) in the main text, with further examples displayed in other panels of the figure.

Fig. S6 shows an additional series of stability functions calculated for a subset of the experimental data by the pointwise division of I_N by $\tilde{I}_N$.
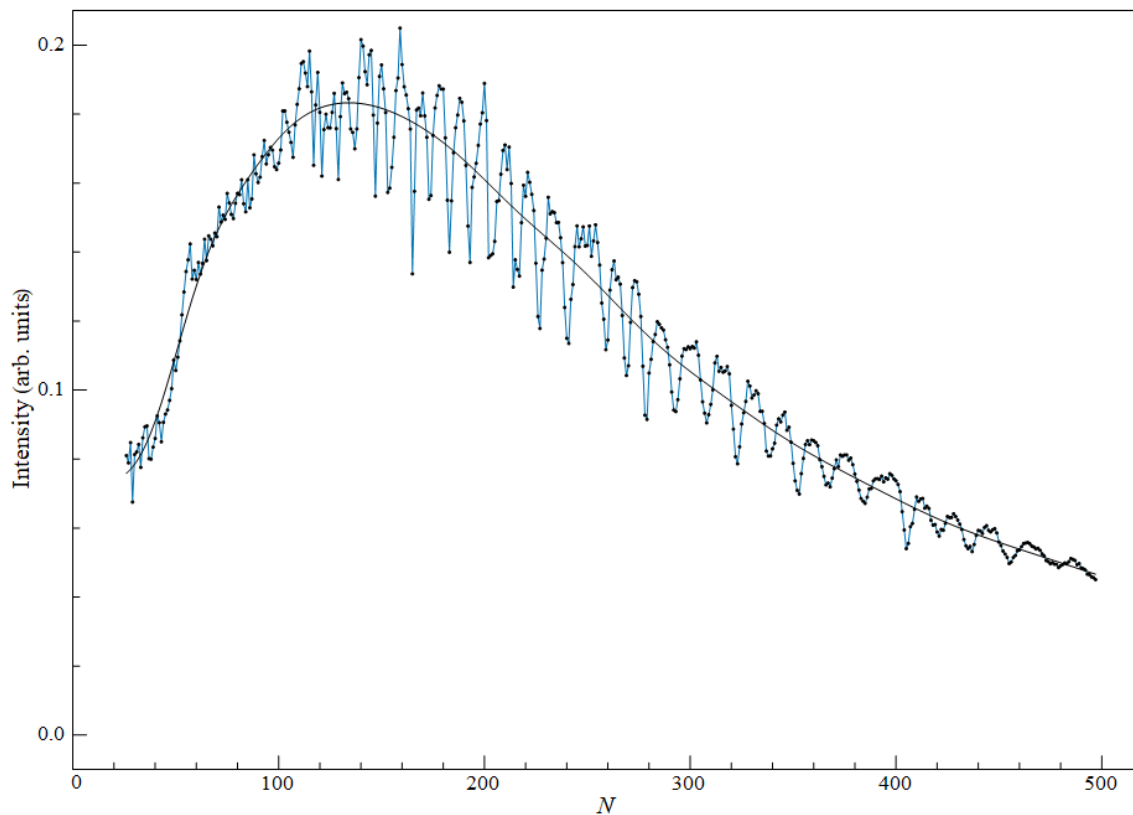
Fig. S5. Dots: integrated intensities of peaks identified in the spectrum of Fig. 2(c) of the main text (see also Fig. S4). Smooth solid curve: their envelope obtained by an iterative Gaussian convolution.
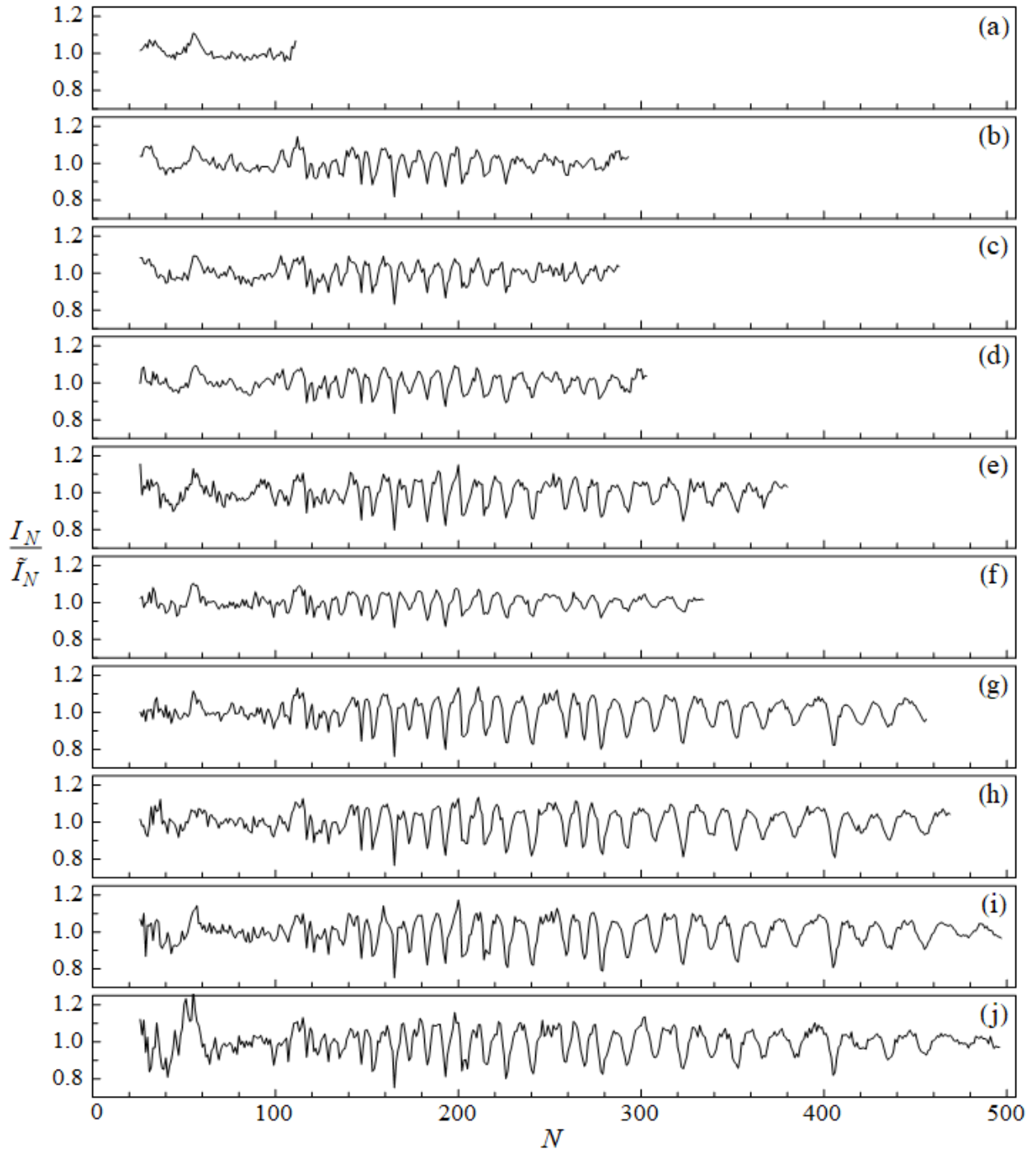
Fig. S6. Stability functions for a data set corresponding to 403 mm nozzle-ionization distance and a range of CO_2 concentrations in the nozzle expansion: (a) 0.38%, (b) 0.69%, (c) 0.77%, (d) 1.00%, (e) 1.54%, (f) 1.61%, (g) 2.31%, (h) 3.08%, (i) 3.85%, (j) 5.02%.

S-III. Gspann parameter

The Gspann parameter, defined as $G_N = \ln(\omega_N t)$, derives from a comparison between an isolated cluster's evaporative rate constant and its experimental flight time. In this way, it relates the maximum microcanonical temperature of an evaporative ensemble to its activation energy.[S5,S6]

The rate constant's frequency prefactor can be written as $\omega_N = \sigma_N \Omega$, where σ_N is the geometrical cross section for the capture of one CO_2 molecule by a cluster of N–1 molecules, $\sigma_N = \pi \left[r_0 (N-1)^{1/3} + r_0 \right]^2$. Here r_0 is the effective radius of one molecule [cf. Eq. (5) in the main text], related to the molecular number density n in the bulk by $n^{-1} = (4\pi/3) r_0^3$. The measured density[S7,S8] yields $r_0 \approx 2.2$ Å.

The parameter Ω can be with good accuracy related to the temperature-dependent bulk vapor pressure P of the cluster material as follows:[S5,S9]

$$P = \Omega \left(\tfrac{1}{8} \pi m k_B T \right)^{1/2} e^{-a/T} . \tag{S.1}$$

Here k_B is the Boltzmann constant, m is the molecular mass, and Ω and a are fitting parameters. Using the tabulated CO_2 pressure data at low temperatures[S8,S10,S11] and plotting $\ln\left(P/\sqrt{T} \right)$ vs. $1/T$ (Fig. S7) we find from the intercept and the above value of r_0 that $\pi r_0^2 \Omega \approx 2.3 \times 10^{16}$ s^{-1}.

We can now compute the value of the Gspann parameter for each cluster N in each data set. The flight time t is derived from the specific set's distance between the nozzle and the mass spectrometer's ionization region, and the measured cluster beam velocity of 540 m/s. For the size range $10 \le N \le 500$ we find that G_N varies between 32 and 35.
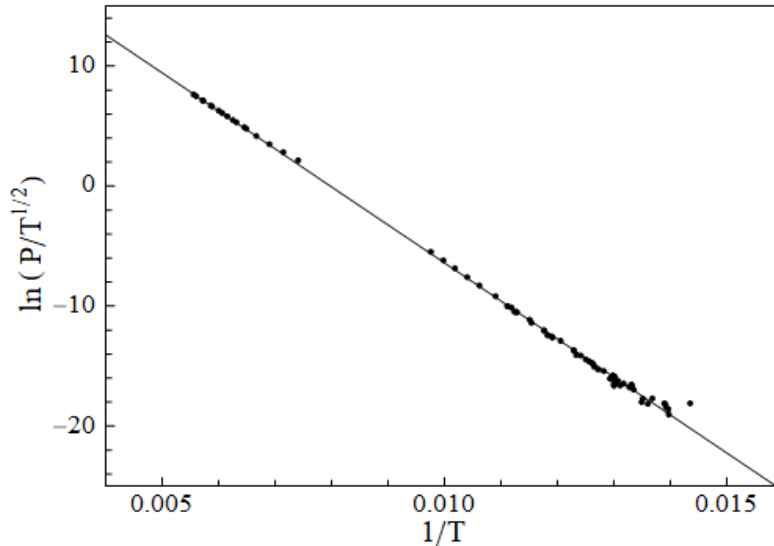
Fig. S7. A plot of CO_2 vapor pressures in the relevant temperature region.

S-IV. Heat capacities

Determination of cluster binding energies from the stability functions requires a knowledge of their heat capacities. These are taken from the molar heat capacity[S10] of bulk CO_2: $C = 4.6k_B$ per molecule at $T \approx 90$ K.

The temperature estimate above is based on using the relation[S5,S6] $T_N \approx D_N/G_N$ and setting $D_N \approx A$, see Eq. (4) in the main text. While variation of the temperature with cluster size could potentially complicate matters, an earlier analysis for water clusters showed that it can be ignored to a good approximation.[S12]

For use in Eq. (1) in the main text we extrapolate the aforementioned bulk heat capacity to finite clusters sizes by setting it to $C(N–2)$ for a cluster of N molecules. The correction in parentheses corresponds to the subtraction of the six rotational and translational degrees of freedom of the whole cluster.

By taking the average of the precursor ($N+1$ molecules) and detected (N molecules) clusters heat capacities, and remembering that the microcanonical heat capacity of isolated clusters in a beam is one k_B less than the canonical value[S13] we obtain $C_N \approx C\left(N-\frac{3}{2}\right)-k_B$.

In Eqs. (2) and (3) in the main text this is employed in dimensionless form, i.e., $C_N \approx 4.6\left(N-\frac{3}{2}\right)-1$.

S-V. Dissociation energies

As described in the main text, Eq. (3) is solved recursively by starting with the value of $I_N/\tilde{I}_N$ for the largest cluster in the data set, and proceeding downward in size. The energy ratio $D_{N+1}/\tilde{D}_{N+1}$ is assigned a starting value near unity, and the equation is iterated to find the energy ratios for all the lower sizes. The procedure converges quickly, and within the space of a few tens of molecules the solutions become insensitive to the precise seed value of the energy ratio. For maximum consistency, we select the seed as follows. It is set to values between 0.90 and 1.10 with an increment of 0.0001, and a corresponding set of energy ratios is computed for each of these values. The set which has the smallest average absolute deviation of $D_N/\tilde{D}_N$ from unity for sizes $N \geq 100$ is selected. We found that the seed values optimized in this way did not deviate from unity by more than a couple of percent.

Fig. S8 shows the energy ratios $D_N/\tilde{D}_N$ derived from the data in Fig. S6.
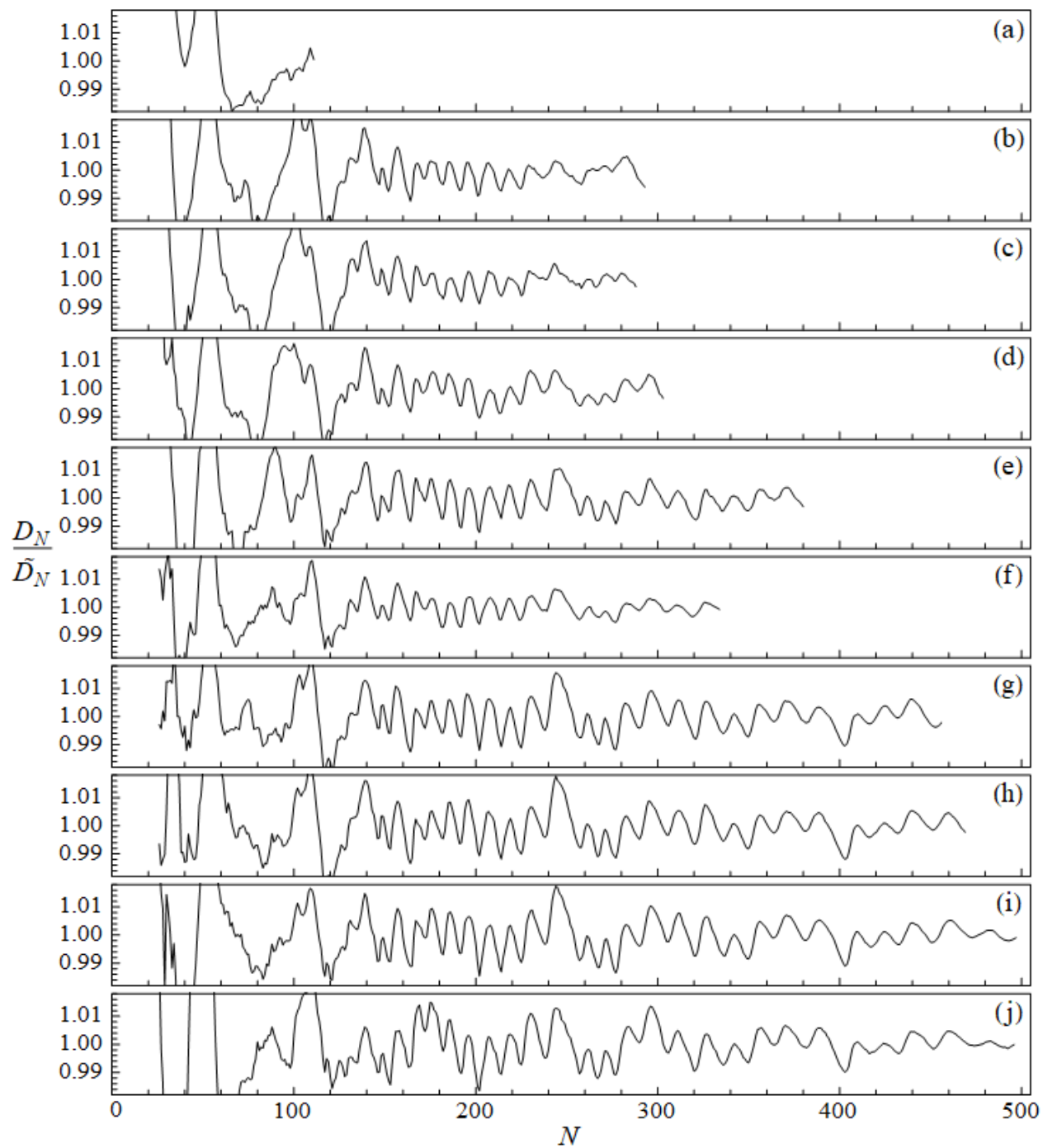
Fig. S8. Dissociation energy ratios derived from the stability functions plotted in Fig. S6.

S-VI. Subshell closings

Fig. S9(a) shows the aggregate set of energy ratios $D_N/\tilde{D}_N$ from Fig. 6(d) in the main text in the region $N \geq 130$. The points of steepest descent are found from this curve by computing the finite difference between successive points, followed by Gaussian smoothing and finally locating the minima, as shown in Fig. S9(b). These cluster sizes, corresponding to sequential facet fillings,[S14] are listed in Table S1 and plotted in Fig. 8 in the main text. These values are the averages of minima candidates obtained by varying the smoothing kernel, and the stated uncertainties derive from the standard deviation of the candidates. A more complicated method involving differentiation of a third order interpolation of the $D_N/\tilde{D}_N$ curve yielded equivalent results.
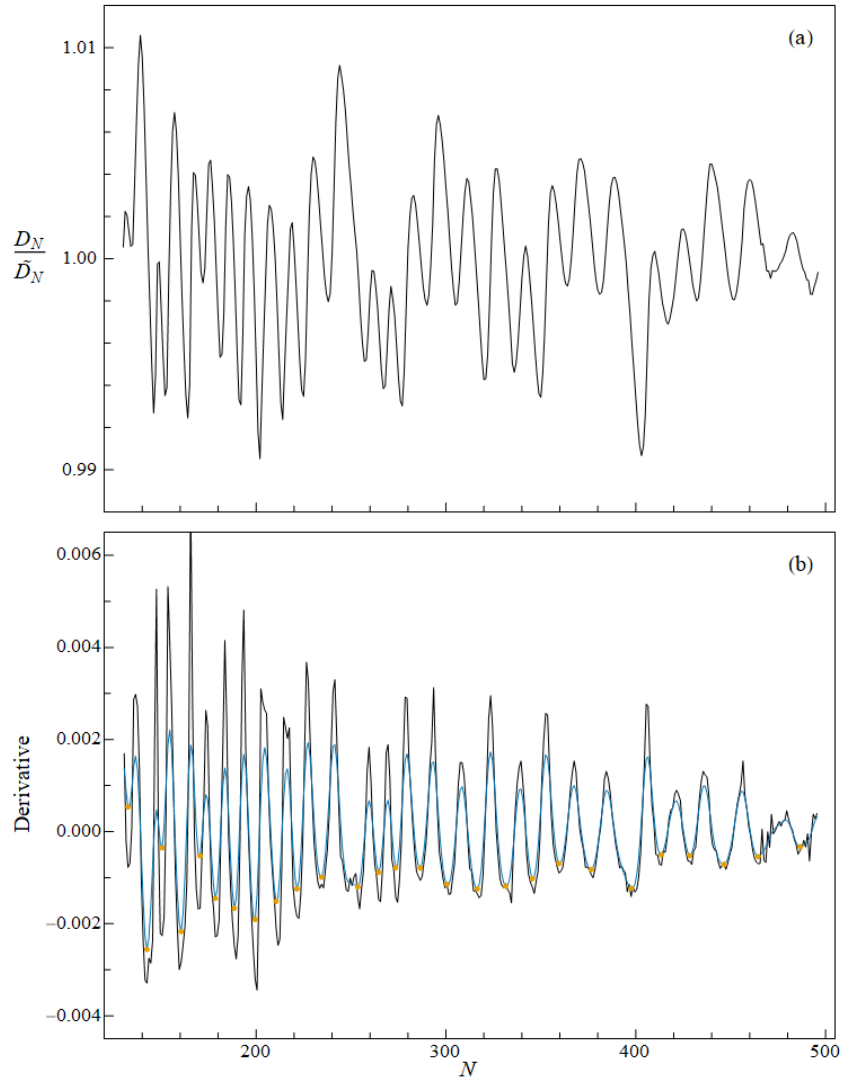
Fig. S9. (a) Energy ratios averaged over the complete data set [Fig. 6(b) in the main text]. (b) Derivative of the plot in the top panel (black curve), its Gaussian smoothing (blue curve) and the minimum points of the latter (yellow dots), identifying the points of steepest descent and thereby the subshell closings.

Table S1. Cluster sizes with subshell closings as determined from the derivative of the aggregate dissociation energy curve.

k'	N_s			k'	N_s		
55	133	±	1	69	287	±	1
56	143	±	1	70	301	±	1
57	151	±	1	71	317	±	1
58	160	±	1	72	333	±	2
59	170	±	1	73	346	±	1
60	179	±	1	74	360	±	1
61	189	±	1	75	377	±	2
62	200	±	1	76	397	±	2
63	211	±	1	77	414	±	1
64	222	±	1	78	429	±	1
65	235	±	1	79	446	±	2
66	252	±	3	80	467	±	3
67	265	±	1	81	488	±	3
68	274	±	1				

S-VII. Geometrical analysis of subshell closings

Refs. S14-S16 discuss the observed oscillating pattern in cluster spectra due to geometrical packing of atoms or molecules. By considering a set of possible polyhedral structures (*fcc* cube, octahedron, decahedron, icosahedron, and cuboctahedron), Negishi *et al.*[S14] concluded that only cuboctahedral clusters represent the mass spectrum of CO_2 clusters on a satisfactory level. However, their analysis neglected shapes such as truncated octahedra and Ino (or Marks) decahedra, which are generally plausible structures for larger atomic clusters.[S17-S20]

In what follows we present the geometrical estimates of subshell closings for cuboctahedral, Ino decahedral, and truncated octahedral clusters with k shells. (Sample clusters for each structure are illustrated in Fig. 8 in the main text and in Fig. S10.)

Cuboctahedron. The total number of monomers in a cuboctahedron with k shells can be written as[S21]

$$N_{\text{cubo}}(k) = \frac{10}{3}k^3 - 5k^2 + \frac{11}{3}k - 1 . \tag{S.2}$$

By means of subshell index $k' = Fk$ (F being the number of facets on a shell) the cube root of N_{cubo} can be developed as a series for large k':

$$N_{\text{cubo}}^{1/3} \approx \frac{(10/3)^{1/3}}{F}(k'-7) + \frac{49}{90^{2/3} Fk}\left(1 + \frac{7}{Fk}\right), \tag{S.3}$$

where the coefficient preceding the first term is about 0.1067 for $F = 14$. The last term of Eq. (S.3) is smaller than 0.05 for the cluster sizes studied here ($k \gtrsim 4$).

Ino decahedron. Ino decahedra are also characterized by the shell index k with an additional parameter p (a positive integer). Geometrically, k and p are the numbers of monomers on the edges between (100) and (111) facets and two (100) facets, respectively [see Fig. S10(b)]. The number of monomers in an Ino decahedron is given by

$$N_{\text{Ino}}(k) = \frac{5}{6}k^3 - \frac{5}{2}k^2 + \frac{8}{3}k + p\left(\frac{5}{2}k^2 - \frac{5}{2}k + 1\right) - 1. \tag{S.4}$$

When $p = k$, a regular Ino decahedron has the number of monomers as a cuboctahedron of k shells. But with $F = 15$ instead of 14, the cube root of N_{Ino} can be expressed to good accuracy by

$$N_{\text{Ino}}^{1/3} \approx \frac{(10/3)^{1/3}}{15}(k'-7.5). \tag{S.5}$$

Thus the prefactor is about 0.100 and the residual term is about 0.05. However, the energetically more favorable clusters have $p < k$ due to a reduced number of monomers on the costly (100) facets. For such Ino decahedra, the highest order term has again a coefficient of ≈ 0.100, but the residual terms for the studied cluster sizes are smaller than ~ 0.025.

Truncated octahedron. The composition of a truncated octahedron differs slightly from the other geometries, and for sake of simplicity an index n (≥ 0) is used instead of the shell index k.

(a) Cuboctahedron: $F = 14$, $k = 6$, $N = 561$

(b) Ino decahedron: $F = 15$, $k = 6$, $p = 4$, $N = 409$

(c) Truncated octahedron: $F = 14$, $n = 3$, $N = 586$
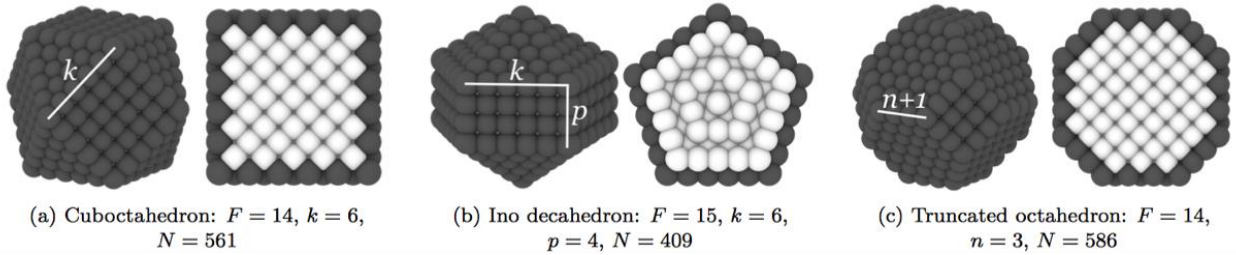
Fig. S10. Examples of the three analyzed geometrical structures. The surface monomers are shown as dark spheres and the core monomers (with a coordination number of 12) as bright ones. The complete structure is shown on the left, and the cross-sectional view is given on the right.

The number of monomers in an "nth" regular truncated octahedron (TO) is

$$N_{TO}(n) = 16n^3 + 15n^2 + 6n + 1, \qquad (S.6)$$

and the number of monomers with a coordination number of 12 (i.e., the number of core monomers) is

$$N_{TO,12}(n) = 16n^3 - 15n^2 + 6n - 1. \qquad (S.7)$$

Based on these two equations and a simple geometrical inspection, the complete depletion of monomers from the surface of the nth truncated octahedron does not produce the $(n–1)$st octahedron but a cluster with $N_{TO}(n) - 30n^2 - 2$ monomers. Thus extra facets are effectively depleted during a full transition from n to $(n–1)$ closed-shell cluster. After the 14 facets are depleted, the amount of excess surface monomers, ΔN, is

$$\Delta N = N_{TO,12}(n) - N_{TO}(n-1) = 18(n^2 - n) + 5. \qquad (S.8)$$

The number of monomers on a subshell of the intermediate cluster can be taken as the average of subshell monomers of the two adjacent closed-shell clusters:

$$\mathcal{N} = \frac{30n^2 + 2 + 30(n-1)^2 + 2}{2 \times 14} \approx 2(n^2 - n). \qquad (S.9)$$

Thus the number of effective facets between the intermediate cluster and the $(n–1)$st cluster is approximately $\Delta N/\mathcal{N} \approx 9$. The total number of facets between two regular truncated octahedra is $F = 23$. For truncated octahedral clusters the cube root of N_{TO} is approximately

$$N_{TO}^{1/3} \approx 0.110(n' + 7) + \frac{0.02n + 0.07}{n}, \qquad (S.10)$$

where the index n' corresponds to k'-14. Thus Eq. (S.10) has a $(k'–7)$ factor similar to Eqs. (S.3) and (S.5). Again the residual term is very small for the relevant cluster sizes ($n \gtrsim 2$).

The geometric analysis for each of the considered structures [Eqs. (S.3), (S.5), and (S.10)] suggests that the subshell index k' is scaled by a factor of $F/2$. This scaling can be explained as resulting from the imperfect indexing of the subshells of the smallest closed-shell cluster. This is demonstrated for the cuboctahedral clusters of $k' \leq 14$ in Fig. S11. Indeed, as shown in the main text, the positions of the subshell closings follow the "cuboctahedral indexing" of $k'–7$.

	(a)	(b)	(c)	(d)	(e)	(f)	(g)
N:	13	9	5	4	3	2	1
k':	14	13	12	11	10	9	8
$k' - 7$:	7	6	5	4	3	2	1
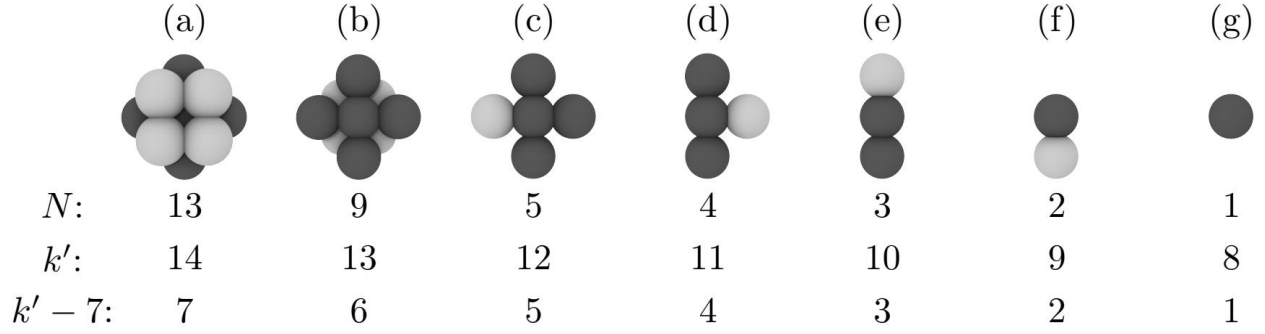
Fig. S11. Subshell indexing of small cuboctahedral clusters. (a) Closed-shell cluster with 13 monomers corresponding to $k=1$ (and $k'=14$). Removal of the four monomers on a (100) facet, indicated as light gray, results in a cluster with 9 monomers and subshell index $k' = 13$ [shown in (b)]. This procedure can be repeated for the subsequent clusters and their facets (being either layers or single monomers) until a single monomer remains (g). The shown sequence of subshell configurations (and the shown values of k') demonstrates that the shifting of k' by 7 results in correct subshell indexing, as for $N=1$ the index $k'-7 = 1$.

S-VIII. Simulation of a peeling-off process

To test the predictive power of the prefactors of the highest-order terms for open-shell structures, we study Lennard-Jones (LJ) clusters with a simple simulation strategy. In our model, the surface monomers on a closed-shell cluster are peeled off one monomer at a time, and after each removal the cluster's energy is minimized using a conjugate gradient algorithm. The monomer to be removed is primarily determined by its coordination number, and secondarily by the minimized energy of the cluster after the monomer removal. Thus the most undercoordinated monomer, whose removal results in the lowest configurational energy, is selected. Note that in this scheme only the surface monomers of the original closed-shell cluster are removed: after a complete depletion of surface monomers a new closed shell remains. The routine is then repeated for the new uncovered closed-shell cluster. A very similar approach was recently used to study the structural motifs of Au clusters.[S20]

It should be also noted that the energy minimization scheme employed here conserves the basic geometry: during the minimization the cluster is not able to collapse into the global minimum (or any other) structure. In the case of LJ clusters consisting of less than 1000 monomers, the global minima exhibit predominantly icosahedral structures.[S22] This is the reason for employing a simple energy minimization instead of an extensive search in phase space using the Hamiltonian.

The stabilities of open-shell clusters are assessed based on the minimized cluster energies E_N with the standard parameters[S21] Δ and Δ_2:

$$\Delta(N) = \frac{E_N - NE_b}{N^{2/3}} \tag{S.11}$$

and

$$\Delta_2(N) = E_{N+1} + E_{N-1} - 2E_N . \tag{S.12}$$

For a LJ crystal the bulk energy of the *fcc* lattice per monomer, E_b, is about -8.6 in standard LJ energy units. The most stable clusters should be located at the local minima and maxima of $\Delta(N)$ and $\Delta_2(N)$, respectively.

The selected starting closed-shell structures are as follows: a cuboctahedron with 561 monomers ($k = 6$), an Ino decahedron with 409 monomers ($k = 6$ and $p = 4$), and a truncated octahedron with 586 monomers ($n = 3$).

The obtained energy parameters Δ and Δ_2 for cluster sizes between $N = 85$ and 409 are shown in Figs. S12(a) and S12(b), respectively. As the peaks appearing in Δ_2 are more distinct than the minima in Δ, these peak positions are considered as the subshell closings N_s. The obtained values of $N_s^{1/3}$ as a function of their order of appearance (corresponding to the subshell index k') are shown in Fig. S11(c). Based on the peeling-off calculations, the geometrical predictions for the highest-order term of N are able to accurately capture the oscillation between the most stable open-shell cluster sizes. However, fluctuations in the values of N_s preclude an accurate analysis of the residuals.

We reiterate that the present model analysis is helpful for identifying the relationship between geometrical structures and the corresponding periodicities of shell and subshell closings. But it should not be used for a direct comparison of cluster configurations and their relative energies between model and experiment because the intermolecular interactions within CO_2 clusters are not sufficiently accurately captured by a coarse-grained LJ model and the peeling-off simulations.
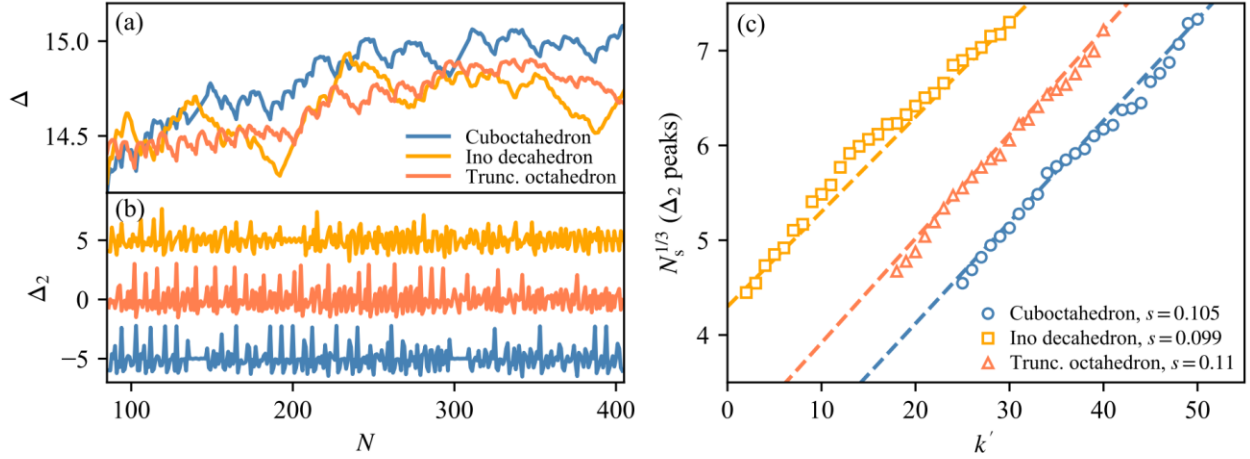
Fig. S12. Results obtained from the peeling-off simulations of LJ clusters having either cuboctahedral, Ino decahedral or truncated octahedral geometries. (a) Energy parameter Δ as a function of cluster size N. (b) Energy parameter Δ_2 for the same clusters. For clarity, the lines for cuboctahedral and Ino decahedral clusters are shifted by -5 and $+5$ energy units, respectively. (c) Cube root of cluster sizes represented by the peaks appearing in Δ_2, as a function of their order of appearance k'. The calculated slopes, s, are given in the legend. The points are arbitrarily shifted so that the largest considered k' considered has a value of either 30, 40, or 50. The theoretical predictions ($s_{cubo} = 0.107$, $s_{Ino} = 0.100$, and $s_{TO} = 0.110$) for these geometries are shown as dashed lines (again allocated according to the largest closing).

References

(S1) M. Lippe, U. Szczepaniak, G.-L. Hou, S. Chakrabarty, J. J. Ferreiro, E. Chasovskikh and R. Signorell, *J. Phys. Chem. A*, 2019, **123**, 2426.

(S2) H. Nishioka, K. Hansen and B. R. Mottelson, *Phys. Rev. B*, 1990, **42**, 9377.

(S3) T. P. Martin, S. Bjørnholm, J. Borggreen, C. Bréchignac, Ph. Cahuzac, K. Hansen and J. Pedersen, *Chem. Phys. Lett*., 1991, **186**, 53.

(S4) A. L. Stancik and E. B. Brauns, *Vib. Spectrosc*., 2008, **47**, 66.

(S5) K. Hansen, *Statistical Physics of Nanoparticles in the Gas Phase*, 2nd ed., Springer Series on Atomic, Optical, and Plasma Physics, Vol. 73, Springer, Dordrecht, 2018.

(S6) R. Rabinovitch, K. Hansen and V. V. Kresin, *J. Phys. Chem. A*, 2011, **115**, 6961.

(S7) W. H. Keesom and J. W. L. Köhler, *Physica*, 1934, **1**, 655.

(S8) *CRC Handbook of Chemistry and Physics*, ed. by J. Rumble, 101st ed., CRC Press, Boca Raton, 2020.

(S9) K. Hansen, Y. Li, V. Kaydashev and E. Janssens, *J. Chem. Phys.*, 2014, **141**, 024302.

(S10) W. F. Giauque and C. J. Egan, *J. Chem. Phys*., 1937, **5**, 45.

(S11) C. E. Bryson, V. Cazcarra and L. L. Levenson, *J. Chem. Eng. Data*, 1974, **19**, 107.

(S12) K. Hansen, P. Andersson and E. Uggerud, *J. Chem. Phys*., 2009, **131**, 124303.

(S13) J. U. Andersen, E. Bonderup and K. Hansen, *J. Chem. Phys*., 2001, **114**, 6518.

(S14) Y. Negishi, T. Nagata and T. Tsukuda, *Chem. Phys. Lett*., 2002, **364**, 127.

(S15) U. Näher, U. Zimmermann and T. P. Martin, *J. Chem. Phys*., 1993, **99**, 2256.

(S16) T. P. Martin, *Phys. Rep.*, 1996, **273**, 199.

(S17) L. D. Marks, *Philos. Mag. A*, 1984, **49**, 81.

(S18) C. L. Cleveland and U. Landman, *J. Chem. Phys.*, 1991, **94**, 7376.

(S19) F. Baletto, R. Ferrando, A. Fortunelli, F. Montalenti and C. Mottet, *J. Chem. Phys*., 2002, **116**, 3856.

(S20) A. L. Garden, A. Pedersen and H. Jónsson, *Nanoscale*, 2018, **10**, 5124.

(S21) F. Baletto and R. Ferrando, *Rev. Mod. Phys*., 2005, **77**, 371.

(S22) J. P. K. Doye and F. Calvo, *J. Chem. Phys.*, 2002, **116**, 8307.